Atmos. Chem. Phys. Discuss., 13, 24301–24342, 2013
www.atmos-chem-phys-discuss.net/13/24301/2013/
doi:10.5194/acpd-13-24301-2013

Atmospheric Chemistry and Physics Discussions

Global distributions and trends of atmospheric ammonia (NH_3) from IASI satellite observations

M. Van Damme[1,2], L. Clarisse[1], C. L. Heald[3], D. Hurtmans[1], Y. Ngadi[1], C. Clerbaux[1,4], A. J. Dolman[2], J. W. Erisman[2,5], and P. F. Coheur[1]

[1]Spectroscopie de l'atmosphère, Chimie Quantique et Photophysique, Université Libre de Bruxelles, Brussels, Belgium
[2]Cluster Earth and Climate, Department of Earth Sciences, Vrije Universiteit Amsterdam, Amsterdam, the Netherlands
[3]Department of Civil and Environmental Engineering and Department of Earth, Atmospheric and Planetary Sciences, MIT, Cambridge, MA, USA
[4]UPMC Univ. Paris 06; Université Versailles St.-Quentin; CNRS/INSU, LATMOS-IPSL, Paris, France
[5]Louis Bolk Institute, Driebergen, the Netherlands

Received: 22 July 2013 – Accepted: 1 September 2013 – Published: 16 September 2013

Correspondence to: M. Van Damme (martin.van.damme@ulb.ac.be)

Published by Copernicus Publications on behalf of the European Geosciences Union.

Abstract

Ammonia (NH_3) emissions in the atmosphere have strongly increased in the past decades, largely because of the intensive livestock production and use of fertilizers. As a short-lived species, NH_3 is highly variable in the atmosphere and its concentration is generally small, except in and close to local source areas. While ground-based measurements are possible, they are challenging and sparse. Advanced infrared sounders in orbit have recently demonstrated their capability to measure NH_3, offering a new tool to refine global and regional budgets. In this paper we describe an improved retrieval scheme of NH_3 total columns from the measurements of the Infrared Atmospheric Sounding Interferometer (IASI). It exploits the hyperspectral character of this instrument by using an extended spectral range (800–1200 cm^{-1}) where NH_3 is optically active. This scheme consists of the calculation of a dimensionless spectral index from the IASI level1C radiances, which is subsequently converted to a total NH_3 column using look-up-tables built from forward radiative transfer model simulations. We show how to retrieve the NH_3 total columns from IASI quasi-globally and twice daily, above both land and sea, without large computational resources and with an improved detection limit. The retrieval also provides error characterization on the retrieved columns. Five years of IASI measurements (1 November 2007 to 31 October 2012) have been processed to acquire the first global and multiple-year dataset of NH_3 total columns, which are evaluated and compared to similar products from other retrieval methods. Spatial distributions from the five years dataset are provided and analyzed at global and regional scales. We show in particular the ability of this method to identify smaller emission sources than those reported previously, as well as transport patterns above sea. The five year time series is further examined in terms of seasonality and interannual variability (in particular as a function of fire activity) separately for the Northern and Southern Hemispheres.

ACPD
13, 24301–24342, 2013

1 Introduction

Human activities during the last decades have substantially perturbed the natural nitrogen cycle up to a level that is believed to be beyond the safe operating space for humanity (Galloway et al., 2008; Rockström et al., 2009, and references therein). Similar to the carbon cycle, anthropogenic perturbations of the nitrogen cycle originate from production of energy and food to sustain human populations which causes the release of reactive nitrogen compounds (collectively abbreviated as Nr), principally in the form of nitrogen oxides ($NO_x = NO+NO_2$), nitrous oxide (N_2O), nitrate (NO_3) and ammonia (NH_3).

The Nr released into the environment is dispersed by hydrologic and atmospheric transport processes and can also accumulate locally in soils, vegetation, and groundwater (Galloway et al., 2008). Excess Nr has important impacts on the environment, climate and human health (e.g. Sutton et al., 2011; Erisman et al., 2013) such as loss of biodiversity, vegetation damage and an increasing number of coastal dead zones (Bobbink et al., 2010; Krupa, 2003; Diaz and Rosenberg, 2011). In fact, one single nitrogen atom, moving along its biogeochemical pathway in ecosystems, can have a multitude of negative impacts in sequence (Galloway et al., 2003). This sequential process, known as the "nitrogen cascade", has been described in theory but quantitatively large uncertainties exist on atmospheric emissions as well as chemistry, transport and deposition of Nr. These are such that our knowledge on the environmental impacts is largely incomplete (Galloway et al., 2003; Erisman et al., 2013). It is commonly acknowledged that the major uncertainties are related to reduced nitrogen compounds, and in particular NH_3 (e.g. Sutton et al., 2011; Erisman et al., 2007; Fowler et al., 2013).

It was estimated that in 2008 about 49.3 Tg of NH_3 was emitted in the atmosphere, and that on a global basis 81 % of this amount was related to agriculture: 58 % to agricultural soils, 21 % to manure management and 2 % to agricultural burning. The second most important source are vegetation fires, which contribute to 16 % to the global emissions, with substantial year-to-year variability (EDGAR-Emission Database

ACPD
13, 24301–24342, 2013

for Global Atmospheric Research, 2011). In addition, the relative importance of the emission sources can show large variations at local and regional scales: for instance combustion associated with catalytic converters could contribute up to 10 % of the yearly emissions in US (Reis et al., 2009); in Europe the agricultural sector accounts for around 94 % of the NH_3 emissions (EEA-European Environment Agency, 2012).

In the atmosphere NH_3 is a highly reactive and soluble alkaline gas. Reactions with components formed from the primary gases NO_x, sulphur dioxide (SO_2), and hydrochloric acid (HCl) form secondary ammonium (NH_4^+) particles, which are important components of atmospheric aerosols of anthropogenic origin (Seinfeld, 1986; Pinder et al., 2008). In this respect, model studies have shown that a reduction of secondary particulate matter in Europe could only be effectively achieved by reducing NH_3 emissions in addition to the reduction of other primary gases (Erisman and Schaap, 2004). The large uncertainties in emissions combined with the complexity associated with modeling aerosol formation, are such that current models do not satisfactorily reproduce atmospheric measurements of NH_3. They exhibit a general tendency to underestimate the concentrations, at least in the industrialized Northern Hemisphere (Heald et al., 2012).

Observing the spatial and temporal distribution of atmospheric NH_3 is therefore essential to better quantify emissions, concentrations and depositions and to develop and evaluate relevant management strategies for the future. Until recently, all the available techniques used surface instrumentations (Erisman et al., 2007), which only allow local studies. Furthermore, these surface automated measuring devices are expensive and not always reliable, putting a limit on what can be expected from these in situ measurements (Erisman et al., 2003; Laj et al., 2009). It is worth noting that airborne (e.g. Nowak et al., 2007, 2010) as well as ship (e.g. Norman and Leck, 2005; Sharma et al., 2012) NH_3 measurements have been also reported but are restrained to campaigns limited in time and spatial coverage. The recently discovered capability of advanced IR-sounders to probe atmospheric NH_3 (Beer et al., 2008; Coheur et al., 2009; Clarisse et al., 2009, 2010; Shephard et al., 2011) is an important step forward in solving this ob-

ACPD
13, 24301–24342, 2013

servational gap. In particular the Infrared Atmospheric Sounding Interferometer (IASI), which is aboard the European MetOp polar orbiting satellites, offers the potential for monitoring NH_3 distributions globally and on a daily basis. This capability stems on the one hand from its scanning mode and on the other hand from its unprecedented hyperspectral and radiometric specifications. The first global distributions were acquired by IASI in 2009 following a simplified retrieval method (Clarisse et al., 2009) and by averaging the retrieved columns over a full year. In a subsequent case study of the San Joaquin Valley (Clarisse et al., 2010), a better understanding was achieved of what can be done with space based measurements, and of the different parameters that affect measurement sensitivity (especially skin and atmospheric temperatures). Walker et al. (2011) introduced an innovative detection method, which substantially improves the NH_3 detection sensitivity of IASI. The availability of the satellite NH_3 measurements, from IASI or the Tropospheric Emission Spectrometer (TES) has triggered work on particulate inorganic nitrogen in the United States: Heald et al. (2012) and Walker et al. (2012) used for this purpose one complete year of IASI measurements and a series of TES measurements respectively, in combination with the GEOS-Chem model. IASI measurements also allowed to confirm the importance of agricultural sources for anthropogenic dust and the non neligible role of NH_3 in their properties (e.g. lifetime) (Ginoux et al., 2012).

The present paper describes an improved retrieval scheme for near-real-time global NH_3 retrievals from IASI building on the work of Walker et al. (2011). It allows retrieving NH_3 total columns from IASI with a better sensitivity on a single measurement and on a bi-daily basis (i.e. using both the night-time and daytime measurements); importantly we also provide an appropriate error characterization. In the next section we first review some of the main characteristics of IASI. In Sect. 3, the retrieval method is thoroughly described and its advantages are discussed against other existing retrieval schemes, especially the Fast Optimal Retrieval on Layers for IASI (Hurtmans et al., 2012). Section 4 provides an analysis of the global distributions of NH_3 acquired with this new retrieval method, underlining the improved sensitivity by the identification of

ACPD
13, 24301–24342, 2013

new hotspots. In this last section the trends in NH_3 concentrations over five years of IASI operation are presented and discussed.

2 The Infrared Atmospheric Sounding Interferometer (IASI)

IASI is an infrared Fourier transform spectrometer launched first aboard MetOp-A in October 2006 and operating since then, with remarkable stability (Hilton et al., 2012). A second instrument is in operation on MetOp-B since September 2012, but here only the IASI-A measurements are analyzed. IASI combines the heritage of weather forecasting instruments with that of tropospheric sounders dedicated to atmospheric chemistry and climate (Clerbaux et al., 2009; Hilton et al., 2012). It circles in a polar sun-synchronous orbit and operates in a nadir-viewing mode with overpass times at 09:30 (hereafter referred to as daytime measurements) and 21:30 (night-time measurements) local solar times when it crosses the equator. The nadir views are complemented by measurements off-nadir along a 2100 km wide swath perpendicular to the flight line. With a total of 120 views along the swath, IASI provides near global coverage two times a day. It has a square field of view composed of four circular footprints of 12 km each at nadir, distorting to ellipse-shaped pixels off-nadir. IASI measures the infrared radiation emitted by the Earth surface and the atmosphere in the 645–2760 cm^{-1} spectral range at a medium spectral resolution of 0.5 cm^{-1} apodized and low noise (~0.2 K at 950 cm^{-1} and 280 K) (Clerbaux et al., 2009). The spectral performance and high spatial and temporal sampling makes IASI a powerful sounder to monitor atmospheric composition, with routine measurements of greenhouse gases and some reactive species (in particular CO, O_3, HNO_3) and observations of other short-lived species, including NH_3, above source regions or in very concentrated pollution plumes. In total 24 atmospheric species have been identified in the IASI spectra (Clarisse et al., 2011).

ACPD
13, 24301–24342, 2013

3 Retrievals of NH_3 from IASI

3.1 Overview of retrieval schemes and spectral ranges

NH_3 is detected in the thermal infrared spectral range in its ν_2 vibrational band centred at around 950 cm^{-1} (Beer et al., 2008; Coheur et al., 2009). While many spectral features are potentially usable in the spectral range between 750 and 1250 cm^{-1} (Fig. 1), the early retrievals from TES and IASI have only used part of the available spectral information. TES retrievals (Shephard et al., 2011), which are based on an optimal estimation strategy and provide weakly-resolved profiles, exploit for instance only a set of micro-windows within the strong Q-branch between 960 and 970 cm^{-1}, while the first global distributions from IASI were acquired using a brightness temperature difference based on a single NH_3 feature at 867.75 cm^{-1} (orange in Fig. 1) (Clarisse et al., 2009). Near-real-time distributions of NH_3 were later obtained from the Fast Optimal Retrieval on Layers for IASI (FORLI) processing chain described elsewhere in detail for CO, O_3 and HNO_3 profiles (Hurtmans et al., 2012). FORLI relies on a full radiative transfer model using the optimal estimation method for the inverse scheme and for the NH_3 profile retrievals it uses specifically a priori constraints from the TM5 model and a spectral range from 950 to 979 cm^{-1} (green range in Fig. 1). FORLI retrievals are, however, only performed on the IASI spectra from the morning orbit and for which the NH_3 signal is clearly detected in a first step. This results in a limited number of retrievals per day, which favor high concentrations (an example is provided in Fig. 2). Preliminary usage of the FORLI-NH_3 retrieved profiles for model studies also revealed difficulties in using the averaging kernels (Heald et al., 2012), which are too low and not representative of the available information in the measurements as a consequence of the retrieval settings chosen to ensure stability and convergence with the optimal estimation framework.

The retrieval scheme we developed avoids these weaknesses. One element of our improved retrieval algorithm relies on the detection algorithm of Walker et al. (2011)

ACPD
13, 24301–24342, 2013

which allows using a large spectral range. In fact we even extend the 800–1000 cm^{-1} range (red range in Fig. 1) used in Walker et al. (2011) to 800–1200 cm^{-1} (dark blue range in Fig. 1). The second element of our improved algorithm is akin to the brightness temperature differences to column conversion from Clarisse et al. (2009), but this time taking fully into account the dependency of the NH_3 spectral signature on thermal contrast.

3.2 A retrieval scheme based on the calculation of Hyperspectral Range Index

The retrieval scheme presented here is built on the detection method described by Walker et al. (2011), which can detect trace gases better than any other known method. It works especially well for those which are only sometimes seen in IASI spectra. The first step is an extension of this detection method and consists in calculating a so-called Hyperspectral Range Index (*HRI* hereafter) from each IASI observation; in the second step the *HRI* is converted into a NH_3 total column using large look-up-tables built from forward radiative transfer calculations under various atmospheric conditions. The two steps are successively detailed below.

3.2.1 Hyperspectral Range Index (*HRI*)

As opposed to brightness temperature differences (ΔBT), which usually rely on a single specific spectral channel in which the target species is optically active, the *HRI* takes into account a broad spectral range to increase sensitivity. For NH_3 from IASI we consider almost the entire ν_2 vibrational band, from 800 to 1200 cm^{-1} (dark blue range in Fig. 1). The method developed in Walker et al. (2011) relies on optimal estimation formalism (Rodgers, 2000), but with a generalized noise covariance matrix that contains in addition to the usual instrumental noise the entire expected spectral variability due to all atmospheric parameters except NH_3. In the spectral range selected here, the variability is associated mainly with temperature, ozone, water, clouds and surface emissivity. In addition to lowering the detection threshold, the method has the advan-

ACPD
13, 24301–24342, 2013

tage of providing in a single retrieval step (this assumes linearity of the NH_3 signature around a vanishingly small abundance) a quantity that is representative of the NH_3 abundance, without having to retrieve other parameters. It is this quantity that we refer to as the *HRI*. It is similar, other than units, to the apparent column retrieved in Walker et al. (2011).

More specifically, we first construct a mean background spectrum $\overline{\boldsymbol{y}}$ and associated variance-covariance matrix $\mathbf{S}_y^{\mathrm{obs}}$ from spectra which are assumed to have no detectable NH_3 signature. With these, the *HRI* of a measured spectrum $\boldsymbol{y}$ is defined as

$$HRI = \mathbf{G}(\boldsymbol{y} - \overline{\boldsymbol{y}}). \quad (1)$$

With $\mathbf{G}$ the measurement contribution function

$$\mathbf{G} = \left(\mathbf{K}^T \mathbf{S}_y^{\mathrm{obs}\,-1} \mathbf{K}\right)^{-1} \mathbf{K}^T \mathbf{S}_y^{\mathrm{obs}\,-1}. \quad (2)$$

Here $\mathbf{K}$ is the difference between a spectrum simulated with a given (small) amount and a spectrum simulated without NH_3. For the forward model, the Atmosphit software was used (Coheur et al., 2005). With these definitions, $\mathbf{K}$ and $\mathbf{G}$ have respectively radiance and inverse radiance units. The *HRI* is as a matter of consequence dimensionless and will be either positive or negative depending on the sign of $\mathbf{K}$ (positive for an absorption spectrum and negative for an emission spectrum).

For the calculation of $\overline{\mathbf{y}}$ and $\mathbf{S}_y^{\mathrm{obs}}$ we used a subset of the IASI spectra measured on 15 August 2010 (around 640 000 spectra in total), in which no NH_3 was detected. To select spectra with no detectable ammonia signature, we used an iterative approach (Clarisse et al., 2013). First, all spectra showing a significant brightness temperature difference at 867.75 cm^{-1} ($\Delta\mathrm{BT} > 0.25$ K) were excluded (Clarisse et al., 2009). Second, from the remaining set, an initial variance-covariance matrix $\mathbf{S}_y^{\mathrm{obs}}$ was built using the spectral interval between 900 and 970 cm^{-1} and the *HRI* calculated a first time. Finally, the spectra with a measurable *HRI* were removed to build a new $\mathbf{S}_y^{\mathrm{obs}}$ between 800 and 1200 cm^{-1}, which ultimately includes around 500 000 NH_3-free measurements.

ACPD
13, 24301–24342, 2013

The conversion of the *HRI* to total columns of NH_3 is not straightforward and requires full radiative transfer simulations. In our method, the conversion is done using theoretical look-up-tables (LUTs) to achieve fast processing of the IASI dataset from 2007 to the present.

3.2.2 Look-up-tables

The LUTs were built by simulating a large amount of IASI spectra using a climatology of 4940 thermodynamic atmospheric profiles above land and 8904 profiles above sea (Chevallier, 2001) with the Atmosphit line-by-line radiative transfer model. For these two categories a reference NH_3 vertical profile was used (Fig. 3), which was constructed from a series of GEOS-Chem (www.geos-chem.org) v8.03.01 model profiles representative of polluted (for the land) and transported (for the sea) conditions in 2009 at $2^\circ \times 2.5^\circ$ horizontal resolution. Model simulations were used as a substitute for representative NH_3 measured profiles which are not available. Figure 3 shows that the land standard profile peaks at the surface and decreases rapidly with altitude, whereas the ocean profile has its maximum at around 1.4 km. To include in the LUTs a representative set of NH_3 concentrations, the profiles were scaled by 13 different values from 0 to 10 (0; 0.1; 0.3; 0.5; 1; 1.5; 2.0; 3.0; 4.0; 5.0; 6.5; 8.0; 10.0) for the ocean and by 30 different values from 0 to 200 (0; 0.1; 0.3; 0.5; 1.0; 1.5; 2.0; 2.5; 3.0; 4.0; 5.0; 6.5; 8.0; 10; 12.5; 15; 20; 25; 30; 35; 42.5; 50; 62.5; 75; 87.5; 100; 125; 150; 175; 200) for the land. The largest concentrations for the simulations thus correspond to a concentration at the surface of close to 185 ppb.

In addition to the varying NH_3 concentrations, a critical dimension in the LUTs is the thermal contrast near the surface, which drives the sensitivity of the infrared measurements to boundary layer concentrations (e.g. Clarisse et al., 2010; Bauduin et al., 2013; Deeter et al., 2007). It is defined here as the difference between the skin (surface) temperature and that of the air at an altitude of 1.5 km. While the climatology of Chevallier (2001) encompasses a range of thermal contrasts, it does not include enough variability for the large values that are the most favorable for probing NH_3

ACPD
13, 24301–24342, 2013

(Clarisse et al., 2010). To ensure enough simulations for the larger thermal contrasts the surface temperature was artificially changed for each of the atmospheric profiles to provide reference cases characterized by thermal contrasts up to −20 to +20 K for the sea and −20 to +40 K for the land.

With these inputs, around 450 000 and 116 000 IASI spectra were simulated for land and sea respectively, from which theoretical *HRI* values were calculated following Eq. (1). The LUTs, calculated independently for land and sea, links the *HRI* to the NH_3 column concentration (in molec cm^{-2}) and thermal contrast (K). This is achieved by averaging all the NH_3 columns in a box determined by a given thermal contrast and a given *HRI* plus/minus an estimated error on each. The error on the thermal contrast (TC) is taken as $\sqrt{2} \times 1$ K (considering that both the skin and air temperature have an uncertainty of about 1 K (Pougatchev et al., 2009)) while the error on the *HRI* was taken as 0.0306, which corresponds to the standard deviation of *HRI* calculated for spectra above an area without NH_3 (20–30° N, 30–40°W) for a period of 6 days (1–2–3/05/2010 and 1–2–3/10/2010). The resulting LUTs are depicted in Fig. 4. It shows that a given *HRI* can be associated with different values of the NH_3 column, depending on thermal contrast: for values of thermal contrasts close to zero, the *HRI* is almost vanishing (indicating a signal below the measurement noise) and basically all values of NH_3 total columns are possible for a narrow *HRI* range. In contrast, for the largest values of TC, there is a one-to-one correspondence between *HRI* and the NH_3 column. This dependency appears very clearly also in the estimated errors (right panel in Fig. 4), which are calculated as the standard deviation of the NH_3 columns inside the box defined previously. Errors are the largest (above 100 %) for low values of TC and/or *HRI*, but above land they are generally well below 25 % for TC above a few K and *HRI* larger than 0.5. Above sea, the *HRI* does not include large values (because the concentration range included in the forward simulations is smaller) but the relative errors follow the same behavior.

Considering a detection threshold defined as 2σ on the *HRI*, an indicative total column detection threshold of NH_3 as a function of thermal contrast can be calculated

ACPD
13, 24301–24342, 2013

using the LUTs. The result is shown in Fig. 5 separately for land (red curve) and for sea (blue curve). It indicates that when the contrast in temperature is low (a value of −2.9 K for TC at 1.5 km corresponds to an almost vanishing contrast between the surface and the air just above it) the measurement is insensitive to even very high concentrations of NH_3. For the more favorable values of TC the IASI measurements should in contrast be able to measure NH_3 down to the 10^{16} molec cm^{-2} level.

3.2.3 Global processing of IASI data

The *HRI* are calculated following Eq. (1) from the IASI Level1C radiance spectra, using the meteorological level 2 information from the operational IASI processor (August et al., 2012) to calculate the thermal contrast. Note that occasionally the meteorological Level2 contain a complete temperature profile but no surface temperature. To not lose valuable data, we retrieve for these scenes the surface temperature directly from the spectra using window channels at 957 and 2143 cm^{-1} (keeping the highest value) and the spectral emissivity database provided by Zhou et al. (2011). An example of processing is shown in Fig. 6 for the same day (15 August 2010, morning overpass time) as in Fig. 2. *HRI* distribution (top-left, Fig. 6) depicts a global coverage with highest values over Eastern Europe and Russia associated to the fire event in 2010. Thermal contrast (top-right, Fig. 6) is positive and high for low- and mid-latitude and lower at higher latitude. It is negative above Antarctica and part of Greenland. Data filtering is needed to remove unreliable columns from the NH_3 distribution. The bottom panel of Fig. 6 shows data only for the scenes that have a cloud fraction below 25 % and a surface temperature above 265.15 K. A more strict data filtering could be carried out by the error (bottom-left, Fig. 6) to exclude unreliable columns, as for example the high measurements observed above Greenland or Antarctica. The comparison between Figs. 2 (FORLI optimal estimation scheme) and 6 (our new *HRI* based retrieval scheme) reveal a significant additional number of daily retrieved NH_3 column values. As an indication, even considering only values with an error below 50 % this yield a net gain of 16 082 measurements (or an additional 63 % number of measurements).

ACPD
13, 24301–24342, 2013

4 Results and discussion

4.1 Product evaluation

A first characterization of the product is provided in Fig. 7 with a histogram of the relative error on the retrieved NH_3 column for four different situations, corresponding to land and sea observations, separately for the IASI morning and evening overpasses. The histogram, which is based on five years of observations, shows that the majority of measurements have an error above 75 %. These situations correspond to small values of the *HRI* (small NH_3 column and/or low value of the thermal contrast), and are, as expected, mainly above sea. Retrievals with an error smaller than 75 % are found above land and sea, with a dominance of daytime measurements (especially for the lowest errors), when the thermal contrast is generally positive. As will be shown in Sect. 4.2 (see for example Fig. 10) the NH_3 measurements above sea are all in coastal regions and can be attributed unambiguously to transport from nearby continental sources. Another important conclusion from Fig. 7 comes from the significant number of retrieved columns with errors below 50–75 % during the evening overpass of IASI, and which are very likely associated with temperature inversions at a given altitude within the boundary layer, i.e. negative thermal contrasts, which increase very strongly the sensitivity at that altitude (Clarisse et al., 2010; Bauduin et al., 2013). Finally, we conclude that the retrievals with the lowest errors (smaller than 25 % on the column) are obtained above land for the morning overpass and are associated to a large positive thermal contrast and a significant amount of NH_3.

To test the performance of the different detection methods and retrieval ranges we compare them in terms of sensitivity. As the different quantities (brightness temperature differences and effective retrieved columns) have different units it is useful to look at the noise to signal ratio which is dimensionless. As a measure of the signal we take the mean retrieved value of a collection of 100 spectra with a strong ammonia signature. This value can then be used as a normalization factor for the noise. To measure the noise we take a large collection of spectra with no detectable NH_3 signature

ACPD
13, 24301–24342, 2013

and for which we expect the retrieved (normalized) value (which we called Θ) to be close to zero. The distribution of Θ values for the different detection methods is depicted in Fig. 8. A good measure of the noise to signal ratio is the standard deviation of these distributions. Our newly developed scheme, based on the calculation of the *HRI* provides the smallest standard deviation (0.04), indicating a gain of sensitivity as compared to the other detection methods. The comparison with an *HRI* calculation taking into account a smaller spectral range (800–1000 cm^{-1}, STD = 0.07) indicates the improvement given by the consideration of an extended range (800–1200 cm^{-1}). The improvement is largest in comparison to the first approach presented in (Clarisse et al., 2009), which was based on a simple brightness temperature difference, characterized here by a standard deviation of 0.30.

A quantitative comparison between the NH_3 total columns retrieved from FORLI and the *HRI* scheme presented here is provided in Fig. 9. The comparison is shown separately for one day (15 August 2010 – similar to Figs. 2 and 6 –, left panel) and one year (2011, right panel) of IASI measurements, and is provided as a funtion of the *HRI* retrieval error (color bar). The agreement is excellent (closely matching the 1:1 slope) for the *HRI* retrievals with the smallest errors, as well seen for 15 August, which correspond to the day with very large NH_3 total columns due to the fires in Russia. For the *HRI* derived columns with an error above 50 %, the FORLI retrievals are close to the a priori, indicative for a small NH_3 signature due to either low NH_3 or small values of the thermal contrast. When taken globally, the correlation between the columns retrieved by the two methods is high (Pearson's R coefficient of 0.81 for the year 2011) but with the *HRI* columns on average 35 % lower. Overall the agreement is very good considering the very different approaches, and the dependence of the FORLI retrievals on the a priori. The *HRI* based retrieval scheme removes this dependency, allows retrieval for the daytime and night-time overpasses, above land and sea, and has the valuable advantage of providing an associated error with each observation.

ACPD
13, 24301–24342, 2013

4.2 Global and regional distributions

With the *HRI* retrieval scheme, global distributions of NH_3 have been retrieved from IASI level 1C twice a day over five years of IASI measurements, from 1 November 2007 to 31 October 2012. As the amount of daily data is not always sufficient to obtain meaningful distributions (being determined by the cloud cover and the availability of the temperature profiles from the EUMETSAT operational processing chain), it is for some applications convenient to consider monthly or yearly averages. But averaging is not straightforward as there is a large variability of the error. To tackle this issue, two approaches can be followed: applying a pre-filtering of the measurements by the relative error followed by an arithmetic averaging or using directly a weighted averaging method on the entire dataset. The pre-filtering approach has the advantage of using only those measurements with the lowest error, but will lead naturally to a large bias of the average towards the highest values (for which the error is lower). The weighted averaging method has the advantage of using all of the IASI observations and therefore introduces a smaller bias in the averaging. This is the approach chosen in what is presented next, where the measurements over the period of interest are further gridded in $0.25^\circ \times 0.5^\circ$ cells. The column in each cell is then a weighted average following:

$$\overline{x} = \frac{\sum w_i x_i}{\sum w_i}, \tag{3}$$

where $w_i = 1/\sigma^2$ and σ is the relative error on the retrieved column estimated on a pixel basis. The mean column itself can be assigned an error $\overline{\sigma}$ which is calculated in a similar way as:

$$\overline{\sigma} = \frac{\sum \frac{1}{\sigma_i}}{\sum \frac{1}{\sigma_i^2}}. \tag{4}$$

Figure 10 shows the NH_3 total column distribution in molec cm^{-2} averaged in this way over the five years, separately for the morning (top panel) and evening (bottom panel)

ACPD
13, 24301–24342, 2013

overpass time. Note that to obtain more reliable distributions a post-filtering of the mean columns in the cells has also been carried out: all data with less than 50 (150) measurements per cell and a mean error $\overline{\sigma}$ larger than 75 % (58 %) for the morning orbit above land (sea) have been rejected. The same was done for the evening data, with threshold values of 100 (300) individual observations per cell and 100 % (58 %) on the mean error in the cell. Also the weighted averaging approach using Eq. (3) gives a high contribution to measurements with low relative error and this explains the large impact of fires plumes, as the IASI sensitivity and the NH_3 retrieval scheme efficiency is higher in those cases.

The daytime distribution (top panel in Fig. 10) shows extreme average column values (up to 1.5×10^{17} molec cm^{-2} with error around 60 %) in Russia, which are due to the 2010 large fires, and associated NH_3 emissions, that persisted for several weeks in August 2010 (see R'Honi et al. (2013) and references therein). Other fire related hotspot regions are seen over Alaska (from the 2009 fires), East Russia (2011), South America (mainly from 2010) and Central Africa (throughout 2008–2012).

Most other hotspot regions are related to agriculture. Asia is responsible for the largest NH_3 emissions (EDGAR-Emission Database for Global Atmospheric Research, 2010), especially then over the Indo-Gangetic plain where we found total columns up to 6.4×10^{17} molec cm^{-2} (19 % error). This area is well known for its intensive agricultural practices and its industrial emission (EDGAR-Emission Database for Global Atmospheric Research, 2011). Another hotspot region is the Fergana Valley and the area irrigated by the Syr Daria and the Amu Daria in Uzbekistan and Kazakhstan. These have already been highlighted in previous studies (Scheer et al., 2008; Clarisse et al., 2009), as well as the North China Plain in China (see Fig. 12 and Clarisse et al. (2009)). While many of these larger hotspots have already been identified in our previous study (Clarisse et al., 2009), our new retrieval scheme allows detection of smaller and weaker NH_3 sources. A striking example is the NH_3 detected above regions associated to the development of intensive center-pivot irrigation agriculture in Saudi Arabia, already seen by the LANDSAT instrument (NASA, 2012). Other new

ACPD
13, 24301–24342, 2013

source areas identified in Asia include the mouth of the Shatt al-Arab river (Iraq), Thailand and Indonesia. These are likely caused by biomass burning events on the Borneo and Sumatra Islands (Justice et al., 2011) and intensive fertilizer application on Java Island (Potter et al., 2010).

The distribution in South America is driven by the fire events in 2010 (e.g. center of Brazil), but we can also identify new agricultural hotspots around Santiago (Chile) and in the Llanos area (Colombia, Venezuela) (LADA, 2008; Potter et al., 2010). Two main agricultural source areas show up in North America: the Midwest region and the San Joaquin Valley where high NH_3 columns are observed throughout the year (Clarisse et al., 2010) and up to 6.0×10^{16} molec cm^{-2} (17 % error). NH_3 columns are also now retrieved above Eastern states of the US. Other new source areas are found higher up North for example southeast of Calgary and southeast of Winnipeg (Canada). Both areas are known for their high anthropogenic NH_3 emission (Environment Canada, 2013). In Africa, the largest columns are found over major agricultural regions, especially West Africa (Adon et al., 2010) as well as Sudan and Ethiopia (LADA, 2008). The largest columns were found in Nigeria, where averaged columns up to 2.6×10^{16} molec cm^{-2} (39 % error) were measured. Previously unreported hotspots include the Zambezi basin (Mozambique) and particularly the Bethal/Secunda area (South Africa). The location of the latter suggests industrial emissions as the main source process. The availability of retrievals over Oceania highlights South of Australia and New Zealand, which correspond to the main agricultural land use systems for this continent (LADA, 2008; Potter et al., 2010). In Europe, the highest values are measured above the Po Valley (up to 3.3×10^{16} molec cm^{-2}, 19 % error) and the Netherlands. The improved algorithm is also sensitive above the UK (Sutton et al., 2013) and suggests marked emissions in Eastern Europe.

The night-time measurements show similar hotspots (bottom panel, Fig. 10), however with larger relative errors caused by the general lower thermal contrast for the night-time overpass. On a daily basis, the morning and evening distributions can be quite different as the measurements will be strongly dependent on the local thermal

ACPD
13, 24301–24342, 2013

contrast (in several places, morning and evening measurements bring complementary information). While night-time measurements of NH_3 have been reported before (Clarisse et al., 2010) this is the first time that a global night-time distribution is obtained, which constitutes in itself an important improvement over previous work.

Another major improvement compared to previous studies (both from IASI or TES), is the clear observation of large transported plumes, on the South coast of West Africa, around India and Mexico, and to lesser extent on the East coast of the United States. Atmospheric transport of NH_3 above the Mediterranean and Adriatic sea, emitted from agricultural activities in the Ebro and Po Valley respectively, is also observed by IASI as well as more sporadic transport events on the Plata River (Argentinian coast). These results are spatially consistent with Nr. deposition modeled distributions (Duce et al., 2008) and with NH_x wet deposition simulations (Dentener et al., 2006). A monthly distribution of NH_3 columns (February 2011) is depicted in Fig. 11 showing transported fires plumes on the West and South coast of West Africa (1) and NH_3 transported from agricultural sources on the West coast of India (2), the Bay of Bengal (3) and the Gulf of Guinea (4). The source processes have been attributed by comparing the distribution with fire radiative power (FRP) measurements from the MODerate resolution Imaging Spectroradiometer (MODIS) instrument (Justice et al., 2011). Such export of NH_3 from biomass combustion and other continental sources to ocean has already been reported for Atlantic and Indian Oceans (Norman and Leck, 2005) and for the Bay of Bengal (Sharma et al., 2012) during ship campaigns.

The griding method used for the global distribution in Fig. 10 is not the most suitable for analyzing the NH_3 spatial distributions at smaller scales, as it smooths out some of the finer features. Figure 12 shows a regional NH_3 distribution, taking East Asia as an example, where each column is distributed in the corresponding IASI footprint (circular to ellipse-shaped depending on the angle off nadir) before being averaged in a smaller $0.05^\circ \times 0.05^\circ$ grid following the same method as described above (i.e. error weighted averages, Eq. (3) and (4)). The details of the emission regions are clearly revealed, with larger column values in areas where there is intensive agriculture. This is the case

ACPD
13, 24301–24342, 2013

especially in the Hebei, Henan, Shandong and Jiangsu provinces (North China Plain, 1 in Fig. 12), which altogether account for approximately 30 % of the N fertilizer consumption and 33 % of the crop production in China during the course of 2006 (Zhang et al., 2010; Huang et al., 2012); The North China Plain as a whole is responsible for 43 % of the NH_3 emitted from fertilization in China while it represents only 3.3 % of the national area (Zhang et al., 2010; Huang et al., 2012). Several smaller hotpots are detected in Fig. 12, among which the Sichuan (2) province where the emissions are mainly from livestock, or the Xinjiang province, near Urumqi and in Dzungaria (3) and around the Tarim basin (4), where there is sheep manure management and intensive fertilizer use (Huang et al., 2012; Li et al., 2012). Overall the patterns observed above China are in excellent qualitative agreement with the distribution of sources from the recent emission inventory of Huang et al. (2012).

4.3 Temporal evolution

In addition to the spatial distributions, in Fig. 13 we show the first time series of daily retrieved NH_3 columns above land over the course of the five years, averaged separately for the entire Northern (NH) and Southern Hemisphere (SH). The average values were calculated following Eq. (3), using only the columns measured during the morning orbits of IASI. Higher columns are measured in the Northern Hemisphere (on average for the five years 1.5×10^{16} molec cm^{-2}) as compared to the Southern Hemisphere (1.1×10^{16} molec cm^{-2}), which is mainly due to the dominance of agricultural sources in the Northern part of the globe.

A seasonal cycle is observed in both hemispheres, with peak columns during spring and summer. The seasonality in the Northern Hemisphere is especially pronounced, with columns varying from about 1×10^{16} molec cm^{-2} in winter (from October to February) up the double in spring and summer. The large columns measured throughout August 2010, which increase the average hemispheric column up to 4×10^{16} molec cm^{-2} on 5 August, are due to the large fires in central Russia (see e.g. Fig. 6 and R'Honi et al. (2013)). In the Southern Hemisphere, the seasonal cycle is less marked, the

ACPD
13, 24301–24342, 2013

maximum columns being typically observed there for a three-month period extending from August to October, which corresponds to the biomass burning period in South America and South Africa. In 2010 the emission processes were particularly strong in South America, and the average hemispheric NH_3 value reaches 4.1×10^{16} on 27 August. Note that qualitatively the variations in the NH_3 columns as a function of the fire activity (from year to year) is similar to that observed for carbon monoxide, for which large enhancements in 2010 have in particular been reported (Worden et al., 2013).

5 Conclusions and perspectives

We have described an improved method for the retrieval of NH_3 total column concentrations from IASI spectra, with improved sensitivity and near-real-time applicability. The method follows a two-step process. The first step consists of measuring a so-called Hyperspectral Range Index from each IASI spectrum using an optimal-estimation-like approach, in which the measurement variance-covariance matrix is set to represent the total spectral variability that is not attributable to NH_3. A spectral range extending from 800 to 1200 cm^{-1}, larger than that used in previous studies, was selected and the matrix was built using one day of IASI measurements. In a second step the *HRI* is converted into a total column of NH_3 using look-up-tables (separately for sea and land), built from forward radiative transfer calculations and considering a large number of different atmospheric conditions. The error on the retrieved total columns was estimated from the look-up tables, and shown to be strongly related to the thermal contrast, varying from more than 100 % to lower than 25 % error for the most favorable situations. The latter are usually above land and during daytime, when there is a combination of high thermal contrast and enhanced NH_3. We show that the method retrieves NH_3 with improved sensitivity over previous retrieval schemes. A detailed comparison with the retrieval results from the FORLI software, which uses a full radiative transfer model, showed good agreement overall (correlation coefficient of 0.81, with FORLI biased high by 35 %).

ACPD
13, 24301–24342, 2013

Retrievals of the NH_3 columns for five years of IASI measurements have been performed, from which spatial distributions (separately for morning and evening orbits of IASI) and first time-series have been derived and analyzed. On the five-year average global distributions, a number of new hotspots have been identified, further highlighting the gain of sensitivity over earlier retrieval schemes. Export of NH_3, principally on the West Coast of Africa and around India and Mexico, have been observed for the first time. We have shown with the example of Eastern Asia that the improved retrieval method also detects fine patterns of emissions on the regional scale. Seasonal cycles have been studied from the time series, separately for the Northern and Southern Hemispheres. The seasonality was shown being more pronounced in the Northern Hemisphere, with peak columns in spring and summer. In the Southern Hemisphere, the seasonality is principally related to the biomass burning activity, which causes column enhancements mainly from August to October. The summer 2010 stands out remarkably in the time series in both hemisphere, as a result of the exceptional fires in Russia and in South America and Africa that year.

Currently both MetOp-A and MetOp-B are in operation and so in the short run twice more data will be processed. The IASI program is foreseen to last at least 15 yr and will be followed up by the IASI-NG mission, onboard the MetOp-SG satellite series (Clerbaux et al., 2013). IASI therefore will allow to study global emissions and their long-term trends. Observation of NH_3 export also opens perspectives to assess the NH_3 ocean fertilization and the residence time of this trace gas in this type of plumes. The high spatial and temporal sampling of IASI observations also offers a suitable tool for evaluation of regional and global models. For these purposes, validation (which is on-going) is required and is challenging as both the infrared satellite measurements and of the other monitoring methods each have their own set of limitations. Nevertheless, the complementarities between ground-based, airborne and ship measurements with satellite instruments, and associated modeling efforts, will increasingly allow to better assess the local to global NH_3 budget, distributions and long-term trends.

ACPD
13, 24301–24342, 2013

Acknowledgements. IASI has been developed and built under the responsibility of the "Centre National d'Etudes Spatiales" (CNES, France). It is flown on board the Metop satellites as part of the EUMETSAT Polar System. The IASI L1 data are received through the EUMETCast near real-time data distribution service. The research in Belgium was funded by the F.R.S.-FNRS, the Belgian State Federal Office for Scientific, Technical and Cultural Affairs and the European Space Agency (ESA-Prodex arrangements). Financial support by the "Actions de Recherche Concertées" (Communauté Française de Belgique) is also acknowledged. M. Van Damme is grateful to the "Fonds pour la Formation à la Recherche dans l'Industrie et dans l'Agriculture" of Belgium for a Ph.D. grant (Boursier FRIA). L. Clarisse and P.-F. Coheur are respectively Post-doctoral Researcher and Research Associate (Chercheur Qualifié) with F.R.S.-FNRS. C. Clerbaux is grateful to CNES for scientific collaboration and financial support. C.L. Heald acknowledges funding support from NOAA (NA12OAR4310064). We gratefully acknowledge support from the project "Effects of Climate Change on Air Pollution Impacts and Response Strategies for European Ecosystems" (ÉCLAIRE), funded under the EC 7th Framework Programme (Grant Agreement No. 282910). We would like to thank J. Hadji-Lazaro for her assistance.

References

Adon, M., Galy-Lacaux, C., Yoboué, V., Delon, C., Lacaux, J. P., Castera, P., Gardrat, E., Pienaar, J., Al Ourabi, H., Laouali, D., Diop, B., Sigha-Nkamdjou, L., Akpo, A., Tathy, J. P., Lavenu, F., and Mougin, E.: Long term measurements of sulfur dioxide, nitrogen dioxide, ammonia, nitric acid and ozone in Africa using passive samplers, Atmos. Chem. Phys., 10, 7467–7487, doi:10.5194/acp-10-7467-2010, 2010. 24317

August, T., Klaes, D., Schlüssel, P., Hultberg, T., Crapeau, M., Arriaga, A., O'Carroll, A., Coppens, D., Munro, R., and Calbet, X.: IASI on Metop-A: Operational Level 2 retrievals after five years in orbit, J. Quant. Spectrosc. Radiat. Transfer., 113, 1340–1371, doi:10.1016/j.jqsrt.2012.02.028, 2012. 24312

Bauduin, S., Clarisse, L., Clerbaux, C., Hurtmans, D., and Coheur, P. F.: Observations of suphur dioxide in the planetary boundary layer of Norilsk from the nadir thermal infrared IASI sounder, in preparation, 2013. 24310, 24313

Beer, R., Shephard, M. W., Kulawik, S. S., Clough, S. A., Eldering, A., Bowman, K. W., Sander, S. P., Fisher, B. M., Payne, V. H., Luo, M., Osterman, G. B., and Worden, J. R.: First satellite

ACPD
13, 24301–24342, 2013

observations of lower tropospheric ammonia and methanol, Geophys. Res. Lett., 35, L09801, doi:10.1029/2008GL033642, 2008. 24304, 24307

Bobbink, R., Hicks, K., Galloway, J., Spranger, T., Alkemade, R., Ashmore, M., Bustamante, M., Cinderby, S., Davidson, E., Dentener, F., Emmett, B., Erisman, J.-W., Fenn, M., Gilliam, F., Nordin, A., Pardo, L., and De Vries, W.: Global assessment of nitrogen deposition effects on terrestrial plant diversity: a synthesis, Ecol. Appl., 20:1, 30–59, doi:10.1890/08-1140.1, 2010. 24303

Chevallier, F.: Sampled databases of 60-level atmospheric profiles from the ECMWF analyses, Research Report 4, Eumetsat/ECMWF SAF Programme, 2001. 24310

Clarisse, L., Clerbaux, C., Dentener, F., Hurtmans, D., and Coheur, P.-F.: Global ammonia distribution derived from infrared satellite observations, Nat. Geosci., 2, 479–483, doi:10.1038/ngeo551, 2009. 24304, 24305, 24307, 24308, 24309, 24314, 24316, 24330, 24337

Clarisse, L., Shephard, M., Dentener, F., Hurtmans, D., Cady-Pereira, K., Karagulian, F., Van Damme, M., Clerbaux, C., and Coheur, P.-F.: Satellite monitoring of ammonia: A case study of the San Joaquin Valley, J. Geophys. Res., 115, D13302, doi:10.1029/2009JD013291, 2010. 24304, 24305, 24310, 24311, 24313, 24317, 24318

Clarisse, L., R'Honi, Y., Coheur, P.-F., Hurtmans, D., and Clerbaux, C.: Thermal infrared nadir observations of 24 atmospheric gases, Geophys. Res. Lett., 38, L10802, doi:10.1029/2011GL047271, 2011. 24306

Clarisse, L., Coheur, P.-F., Prata, F., Hadji-Lazaro, J., Hurtmans, D., and Clerbaux, C.: A unified approach to infrared aerosol remote sensing and type specification, Atmos. Chem. Phys., 13, 2195–2221, doi:10.5194/acp-13-2195-2013, 2013. 24309

Clerbaux, C., Boynard, A., Clarisse, L., George, M., Hadji-Lazaro, J., Herbin, H., Hurtmans, D., Pommier, M., Razavi, A., Turquety, S., Wespes, C., and Coheur, P.-F.: Monitoring of atmospheric composition using the thermal infrared IASI/MetOp sounder, Atmos. Chem. Phys., 9, 6041–6054, doi:10.5194/acp-9-6041-2009, 2009. 24306

Clerbaux, C. and Crevoisier, C.: New Directions: Infrared remote sensing of the troposphere from satellite: Less, but better, Atmos. Environ., 72, 24–26, doi:10.1016/j.atmosenv.2013.01.057, 2013. 24321

Coheur, P.-F., Barret, B., Turquety, S., Hurtmans, D., Hadji-Lazaro, J., and Clerbaux, C.: Retrieval and characterization of ozone vertical profiles from a thermal infrared nadir sounder, J. Geophys. Res.-Atmos., 110, D24303, doi:10.1029/2005JD005845, 2005. 24309

ACPD
13, 24301–24342, 2013

Coheur, P.-F., Clarisse, L., Turquety, S., Hurtmans, D., and Clerbaux, C.: IASI measurements of reactive trace species in biomass burning plumes, Atmos. Chem. Phys., 9, 5655–5667, doi:10.5194/acp-9-5655-2009, 2009. 24304, 24307

Deeter, M. N., Edwards, D. P., Gille, J. C., and Drummond, J. R.: Sensitivity of MOPITT observations to carbon monoxide in the lower troposphere, J. Geophys. Res.-Atmos., 112, D24306, doi:10.1029/2007JD008929, 2007. 24310

Dentener, F., Drevet, J., Lamarque, J. F., Bey, I., Eickhout, B., Fiore, A. M., Hauglustaine, D., Horowitz, L. W., Krol, M., Kulshrestha, U. C., Lawrence, M., Galy-Lacaux, C., Rast, S., Shindell, D., Stevenson, D., Van Noije, T., Atherton, C., Bell, N., Bergman, D., Butler, T., Cofala, J., Collins, B., Doherty, R., Ellingsen, K., Galloway, J., Gauss, M., Montanaro, V., Müller, J. F., Pitari, G., Rodriguez, J., Sanderson, M., Solmon, F., Strahan, S., Schultz, M., Sudo, K., Szopa, S., and Wild, O.: Nitrogen and sulfur deposition on regional and global scales: A multimodel evaluation, Global Biogeochem. Cy., 20, GB4003, doi:10.1029/2005GB002672, 2006. 24318

Diaz, R. J. and Rosenberg, R.: Introduction to Environmental and Economic Consequences of Hypoxia, Int. J. Water Resour. D., 27, 71–82, doi:10.1080/07900627.2010.531379, 2011. 24303

Duce, R. A., LaRoche, J., Altieri, K., Arrigo, K. R., Baker, A. R., Capone, D. G., Cornell, S., Dentener, F., Galloway, J., Ganeshram, R. S., Geider, R. J., Jickells, T., Kuypers, M. M., Langlois, R., Liss, P. S., Liu, S. M., Middelburg, J. J., Moore, C. M., Nickovic, S., Oschlies, A., Pedersen, T., Prospero, J., Schlitzer, R., Seitzinger, S., Sorensen, L. L., Uematsu, M., Ulloa, O., Voss, M., Ward, B., and Zamora, L.: Impacts of Atmospheric Anthropogenic Nitrogen on the Open Ocean, Science, 320, 893–897, doi:10.1126/science.1150369, 2008. 24318

EDGAR-Emission Database for Global Atmospheric Research: Results of the emission inventory EDGAR v4.1 of July 2010, http://edgar.jrc.ec.europa.eu, access 13th July 2013, 2010. 24316

EDGAR-Emission Database for Global Atmospheric Research: Source: EC-JRC/PBL. EDGAR version 4.2, http://edgar.jrc.ec.europa.eu (last access: 15 October 2012), 2011. 24303, 24316

EEA-European Environment Agency: Ammonia (NH_3) emissions (APE 003), Assessment published December 2012, acces 15th July 2013, 2012. 24304

Environment Canada: National Pollutant Release Inventory, http://www.ec.gc.ca/inrp-npri/default.asp?lang=En&n=E788969F-1, (last access: 19 July 2013), 2013. 24317

ACPD
13, 24301–24342, 2013

Erisman, J. W. and Schaap, M.: The need for ammonia abatement with respect to secondary PM reductions in Europe, Environ. Pollut., 129, 159 – 163, doi:10.1016/j.envpol.2003.08.042, 2004. 24304

Erisman, J. W., Grennfelt, P., and Sutton, M.: The European perspective on nitrogen emission and deposition, Environ. Int., 29, 311–325, doi:10.1016/S0160-4120(02)00162-9, 2003. 24304

Erisman, J. W., Bleeker, A., Galloway, J., and Sutton, M.: Reduced nitrogen in ecology and the environment, Environ. Pollut., 150, 140 – 149, doi:10.1016/j.envpol.2007.06.033, 2007. 24303, 24304

Erisman, J. W., Galloway, J. N., Seitzinger, S., Bleeker, A., Dise, N. B., Petrescu, A. M. R., Leach, A. M., and de Vries, W.: Consequences of human modification of the global nitrogen cycle, Philos. Trans. R. Soc. Ldn., Ser. B, 368, doi:10.1098/rstb.2013.0116, 2013. 24303

Fowler, D., Coyle, M., Skiba, U., Sutton, M. A., Cape, J. N., Reis, S., Sheppard, L. J., Jenkins, A., Grizzetti, B., Galloway, J. N., Vitousek, P., Leach, A., Bouwman, A. F., Butterbach-Bahl, K., Dentener, F., Stevenson, D., Amann, M., and Voss, M.: The global nitrogen cycle in the twenty-first century, Philos. Trans. R. Soc. Ldn., Ser. B, 368, doi:10.1098/rstb.2013.0164, 2013. 24303

Galloway, J., Aber, J., Erisman, J., Seitzinger, S., Howarth, R., Cowling, E., and Cosby, B.: The Nitrogen Cascade, BioScience, 53, 341–356, 2003. 24303

Galloway, J. N., Townsend, A. R., Erisman, J. W., Bekunda, M., Cai, Z., Freney, J. R., Martinelli, L. A., Seitzinger, S. P., and Sutton, M. A.: Transformation of the Nitrogen Cycle: Recent Trends, Questions, and Potential Solutions, Science, 320, 889–892, doi:10.1126/science.1136674, 2008. 24303

Ginoux, P., Clarisse, L., Clerbaux, C., Coheur, P.-F., Dubovik, O., Hsu, N. C., and Van Damme, M.: Mixing of dust and NH_3 observed globally over anthropogenic dust sources, Atmos. Chem. Phys., 12, 7351–7363, doi:10.5194/acp-12-7351-2012, 2012. 24305

Heald, C. L., Jr., J. L. C., Lee, T., Benedict, K. B., Schwandner, F. M., Li, Y., Clarisse, L., Hurtmans, D. R., Van Damme, M., Clerbaux, C., Coheur, P.-F., Philip, S., Martin, R. V., and Pye, H. O. T.: Atmospheric ammonia and particulate inorganic nitrogen over the United States, Atmos. Chem. Phys., 12, 10295–10312, doi:10.5194/acp-12-10295-2012, 2012. 24304, 24305, 24307

Hilton, F., Armante, R., August, T., Barnet, C., Bouchard, A., Camy-Peyret, C., Capelle, V., Clarisse, L., Clerbaux, C., Coheur, P.-F., Collard, A., Crevoisier, C., Dufour, G., Edwards, D.,

ACPD
13, 24301–24342, 2013

Faijan, F., Fourrié, N., Gambacorta, A., Goldberg, M., Guidard, V., Hurtmans, D., Illingworth, S., Jacquinet-Husson, N., Kerzenmacher, T., Klaes, D., Lavanant, L., Masiello, G., Matricardi, M., McNally, A., Newman, S., Pavelin, E., Payan, S., Péquignot, E., Peyridieu, S., Phulpin, T., Remedios, J., Schlüssel, P.ssel, P., Serio, C., Strow, L., Stubenrauch, C., Taylor, J., Tobin, D., Wolf, W., and Zhou, D.: Hyperspectral Earth Observation from IASI: Five Years of Accomplishments, B. Am. Meteor. Soc., 93, 347–370, doi:10.1175/BAMS-D-11-00027.1, 2012. 24306

Huang, X., Song, Y., Li, M., Li, J., Huo, Q., Cai, X., Zhu, T., Hu, M., and Zhang, H.: A high-resolution ammonia emission inventory in China, Global Biogeochem. Cy., 26, GB1030, doi:10.1029/2011GB004161, 2012. 24319

Hurtmans, D., Coheur, P.-F., Wespes, C., Clarisse, L., Scharf, O., Clerbaux, C., Hadji-Lazaro, J., George, M., and Turquety, S.: FORLI radiative transfer and retrieval code for IASI, J. Quant. Spectrosc. Radiat. Transfer., p. 1391–1408, doi:10.1016/j.jqsrt.2012.02.036, 2012. 24305, 24307

Justice, C. O., Giglio, L., Roy, D., Boschetti, L., Csiszar, I., Davies, D., Korontzi, S., Schroeder, W., O'Neal, K., and Morisette, J.: MODIS-Derived Global Fire Products, in: Land Remote Sensing and Global Environmental Change, edited by: Ramachandran, B., Justice, C. O., and Abrams, M. J., vol. 11 of Remote Sensing and Digital Image Processing, Springer New York, 661–679, doi:10.1007/978-1-4419-6749-7_29, 2011. 24317, 24318

Krupa, S.: Effects of atmospheric ammonia (NH_3) on terrestrial vegetation: a review, Environ. Pollut., 124, 179–221, doi:10.1016/S0269-7491(02)00434-7, 2003. 24303

LADA: Mapping Land Use Systems and global and regional scale for Land Degradation Assessment Analysis, LADA technical report 8, v1.1, edited by: Nachtergaele F. and Petri, M., 2008. 24317

Laj, P., Klausen, J., Bilde, M., Plaß-Duelmer, C., Pappalardo, G., Clerbaux, C., Baltensperger, U., Hjorth, J., Simpson, D., Reimann, S., Coheur, P.-F., Richter, A., Mazière, M. D., Rudich, Y., McFiggans, G., Torseth, K., Wiedensohler, A., Morin, S., Schulz, M., Allan, J., Attié, J.-L., Barnes, I., Birmili, W., Cammas, J., Dommen, J., Dorn, H.-P., Fowler, D., Fuzzi, S., Glasius, M., Granier, C., Hermann, M., Isaksen, I., Kinne, S., Koren, I., Madonna, F., Maione, M., Massling, A., Moehler, O., Mona, L., Monks, P., Müller, D., Müller, T., Orphal, J., Peuch, V.-H., Stratmann, F., Tanré, D., Tyndall, G., Riziq, A. A., Van Roozendael, M., Villani, P., Wehner, B., Wex, H., and Zardini, A.: Measuring atmospheric composition change, Atmos. Environ., 43, 5351–5414, doi:10.1016/j.atmosenv.2009.08.020, 2009. 24304

ACPD
13, 24301–24342, 2013

Li, K. H., Song, W., Liu, X. J., Shen, J. L., Luo, X. S., Sui, X. Q., Liu, B., Hu, Y. K., Christie, P., and Tian, C. Y.: Atmospheric reactive nitrogen concentrations at ten sites with contrasting land use in an arid region of central Asia, Biogeosciences, 9, 4013–4021, doi:10.5194/bg-9-4013-2012, 2012. 24319

NASA: Crop Circles in the Desert, landsat 5 – TM images, http://earthobservatory.nasa.gov/IOTD/view.php?id=77900, (last access: 15 December 2012), 2012. 24316

Norman, M. and Leck, C.: Distribution of marine boundary layer ammonia over the Atlantic and Indian Oceans during the Aerosols99 cruise, J. Geophys. Res.-Atmos., 110, D16302, doi:10.1029/2005JD005866, 2005. 24304, 24318

Nowak, J. B., Neuman, J. A., Kozai, K., Huey, L. G., Tanner, D. J., Holloway, J. S., Ryerson, T. B., Frost, G. J., McKeen, S. A., and Fehsenfeld, F. C.: A chemical ionization mass spectrometry technique for airborne measurements of ammonia, J. Geophys. Res.-Atmos., 112, D10S02, doi:10.1029/2006JD007589, 2007. 24304

Nowak, J. B., Neuman, J. A., Bahreini, R., Brock, C. A., Middlebrook, A. M., Wollny, A. G., Holloway, J. S., Peischl, J., Ryerson, T. B., and Fehsenfeld, F. C.: Airborne observations of ammonia and ammonium nitrate formation over Houston, Texas, J. Geophys. Res.-Atmos., 115, D22304, doi:10.1029/2010JD014195, 2010. 24304

Pinder, R. W., Gilliland, A. B., and Dennis, R. L.: Environmental impact of atmospheric NH_3 emissions under present and future conditions in the eastern United States, Geophys. Res. Lett., 35, L12808, doi:10.1029/2008GL033732, 2008. 24304

Potter, P., Ramankutty, N., Bennett, E. M., and Donner, S. D.: Characterizing the Spatial Patterns of Global Fertilizer Application and Manure Production, Earth Interact., 14, 1–22, doi:10.1175/2009EI288.1, 2010. 24317

Pougatchev, N., August, T., Calbet, X., Hultberg, T., Oduleye, O., Schlüssel, P., Stiller, B., Germain, K. S., and Bingham, G.: IASI temperature and water vapor retrievals – error assessment and validation, Atmos. Chem. Phys., 9, 6453–6458, doi:10.5194/acp-9-6453-2009, 2009. 24311

Reis, S., Pinder, R. W., Zhang, M., Lijie, G., and Sutton, M. A.: Reactive nitrogen in atmospheric emission inventories, Atmos. Chem. Phys., 9, 7657–7677, doi:10.5194/acp-9-7657-2009, 2009. 24304

R'Honi, Y., Clarisse, L., Clerbaux, C., Hurtmans, D., Duflot, V., Turquety, S., Ngadi, Y., and Coheur, P.-F.: Exceptional emissions of NH_3 and HCOOH in the 2010 Russian wildfires,

ACPD
13, 24301–24342, 2013

Atmos. Chem. Phys., 13, 4171–4181, doi:10.5194/acp-13-4171-2013, 2013. 24316, 24319, 24331

Rockström, J., Steffen, W., Noone, K., Persson, A., Chapin, F. S., Lambin, E. F., Lenton, T. M., Scheffer, M., Folke, C., Schellnhuber, H. J., Nykvist, B., de Wit, C. A., Hughes, T., van der Leeuw, S., Rodhe, H., Sorlin, S., Snyder, P. K., Costanza, R., Svedin, U., Falkenmark, M., Karlberg, L., Corell, R. W., Fabry, V. J., Hansen, J., Walker, B., Liverman, D., Richardson, K., Crutzen, P., and Foley, J. A.: A safe operating space for humanity, Nature, 461, 472–475, doi:10.1038/461472a, 2009. 24303

Rodgers, C.: Inverse Methods for Atmospheric Sounding: Theory and Practice, World Scientific, 2000. 24308

Scheer, C., Wassmann, R., Kienzler, K., Ibragimov, N., and Eschanov, R.: Nitrous oxide emissions from fertilized, irrigated cotton (Gossypium hirsutum L.) in the Aral Sea Basin, Uzbekistan: Influence of nitrogen applications and irrigation practices, Soil Biol. Biochem., 40, 290–301, doi:10.1016/j.soilbio.2007.08.007, 2008. 24316

Seinfeld, J.: Atmospheric chemistry and physics of air pollution, John Wiley & Sons, 738 pp., 1986. 24304

Sharma, S. K., Singh, A. K., Saud, T., Mandal, T. K., Saxena, M., Singh, S., Ghosh, S. K., and Raha, S.: Measurement of ambient NH_3 over Bay of Bengal during W_ICARB Campaign, Ann. Geophys., 30, 371–377, doi:10.5194/angeo-30-371-2012, 2012. 24304, 24318

Shephard, M. W., Cady-Pereira, K. E., Luo, M., Henze, D. K., Pinder, R. W., Walker, J. T., Rinsland, C. P., Bash, J. O., Zhu, L., Payne, V. H., and Clarisse, L.: TES ammonia retrieval strategy and global observations of the spatial and seasonal variability of ammonia, Atmos. Chem. Phys., 11, 10743–10763, doi:10.5194/acp-11-10743-2011, 2011. 24304, 24307

Sutton, M. A., Oenema, O., Erisman, J. W., Leip, A., van Grinsven, H., and Winiwarter, W.: Too much of a good thing, Nature, 472, 159–161, doi:10.1038/472159a, 2011. 24303

Sutton, M. A., Reis, S., Riddick, S. N., Dragosits, U., Nemitz, E., Theobald, M. R., Tang, Y. S., Braban, C. F., Vieno, M., Dore, A. J., Mitchell, R. F., Wanless, S., Daunt, F., Fowler, D., Blackall, T. D., Milford, C., Flechard, C. R., Loubet, B., Massad, R., Cellier, P., Personne, E., Coheur, P. F., Clarisse, L., Van Damme, M., Ngadi, Y., Clerbaux, C., Skjøth, C. A., Geels, C., Hertel, O., Wichink Kruit, R. J., Pinder, R. W., Bash, J. O., Walker, J. T., Simpson, D., Horváth, L., Misselbrook, T. H., Bleeker, A., Dentener, F., and de Vries, W.: Towards a climate-dependent paradigm of ammonia emission and deposition, Philos. Trans. R. Soc. Ldn, Ser. B, 368, doi:10.1098/rstb.2013.0166, 2013. 24317

ACPD
13, 24301–24342, 2013

Walker, J. C., Dudhia, A., and Carboni, E.: An effective method for the detection of trace species demonstrated using the MetOp Infrared Atmospheric Sounding Interferometer, Atmos. Meas. Tech., 4, 1567–1580, doi:10.5194/amt-4-1567-2011, 2011. 24305, 24307, 24308, 24309

Walker, J. M., Philip, S., Martin, R. V., and Seinfeld, J. H.: Simulation of nitrate, sulfate, and ammonium aerosols over the United States, Atmos. Chem. Phys., 12, 11213–11227, doi:10.5194/acp-12-11213-2012, 2012. 24305

Worden, H. M., Deeter, M. N., Frankenberg, C., George, M., Nichitiu, F., Worden, J., Aben, I., Bowman, K. W., Clerbaux, C., Coheur, P. F., de Laat, A. T. J., Detweiler, R., Drummond, J. R., Edwards, D. P., Gille, J. C., Hurtmans, D., Luo, M., Martínez-Alonso, S., Massie, S., Pfister, G., and Warner, J. X.: Decadal record of satellite carbon monoxide observations, Atmos. Chem. Phys., 13, 837–850, doi:10.5194/acp-13-837-2013, 2013. 24320

Zhang, Y., Dore, A., Ma, L., Liu, X., Ma, W., Cape, J., and Zhang, F.: Agricultural ammonia emissions inventory and spatial distribution in the North China Plain, Environ. Pollut., 158, 490–501, doi:10.1016/j.envpol.2009.08.033, 2010. 24319

Zhou, D., Larar, A., Liu, X., Smith, W., Strow, L., Yang, P., Schlüssel, P., and Calbet, X.: Global Land Surface Emissivity Retrieved From Satellite Ultraspectral IR Measurements, IEEE T. Geosci. Remote, 49, 1277–1290, doi:10.1109/TGRS.2010.2051036, 2011. 24312

ACPD
13, 24301–24342, 2013

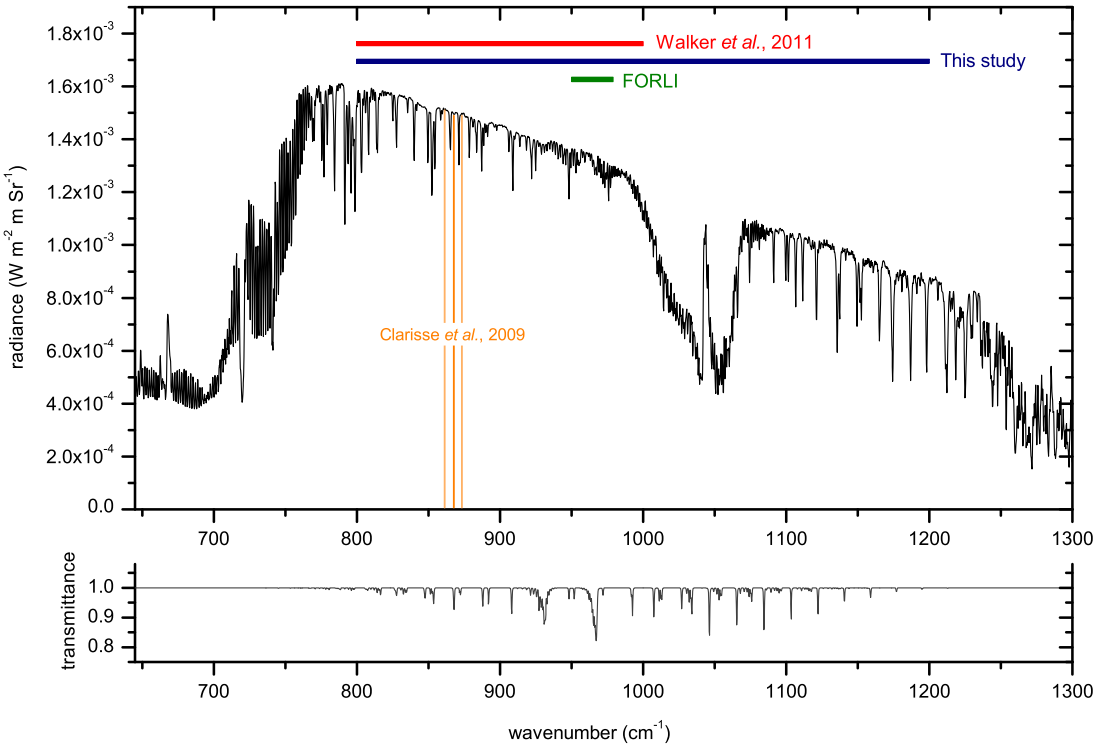

Fig. 1. Top: Example of an IASI spectra between 645 and 1300 cm^{-1} measured on 30 August 2011 in the San Joaquin Valley. The orange range was used for the first global NH_3 distribution obtained by satellite (Clarisse et al., 2009), with the vertical lines representing the channels used to compute the brightness temperature difference. The green range shows the spectral interval used by FORLI. The large red and dark blue ranges are the continuous spectral intervals used for the NH_3 detection in Walker et al. (2011) and in this work, respectively. Bottom: Transmittance of ν_2 vibrational band of NH_3.

ACPD
13, 24301–24342, 2013

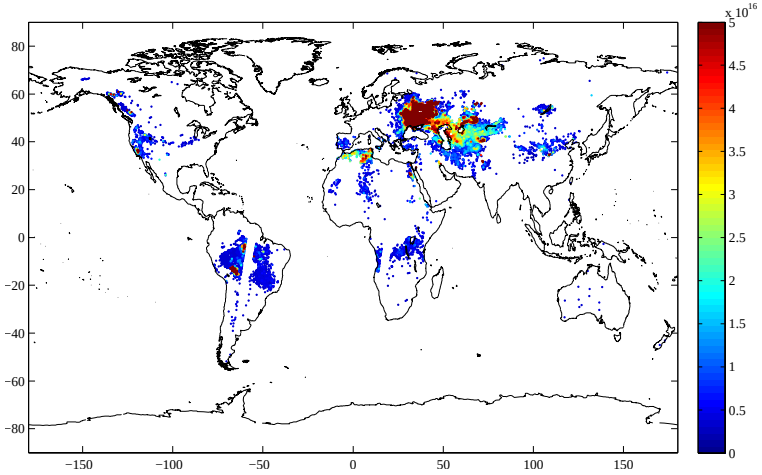

Fig. 2. IASI morning NH_3 observations (molec cm^{-2}) on 15 August 2010 obtained using the FORLI processing chain. The high concentrations measured in Eastern Europe are due to the exceptional emissions from the large Russian fires in the summer of 2010 (R'Honi et al., 2013).

ACPD
13, 24301–24342, 2013

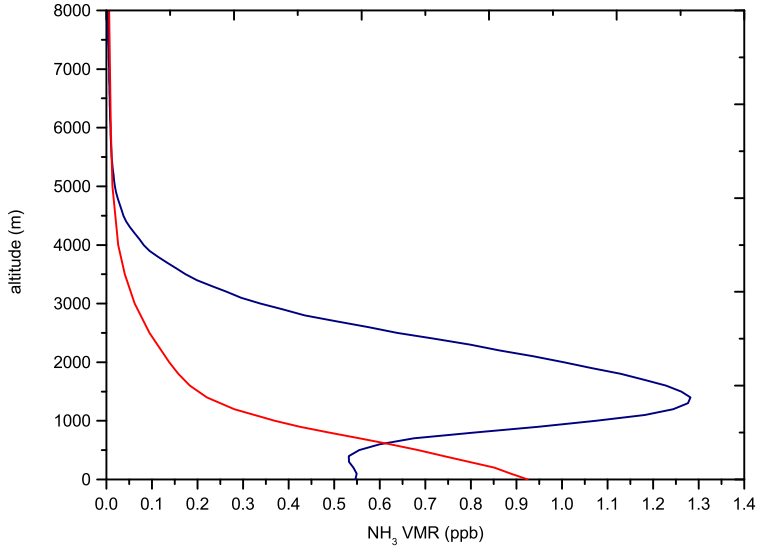

Fig. 3. NH_3 GEOS-Chem model profiles above a source area (red) and transported above sea (blue), used as reference for the radiative transfer simulations.

ACPD
13, 24301–24342, 2013

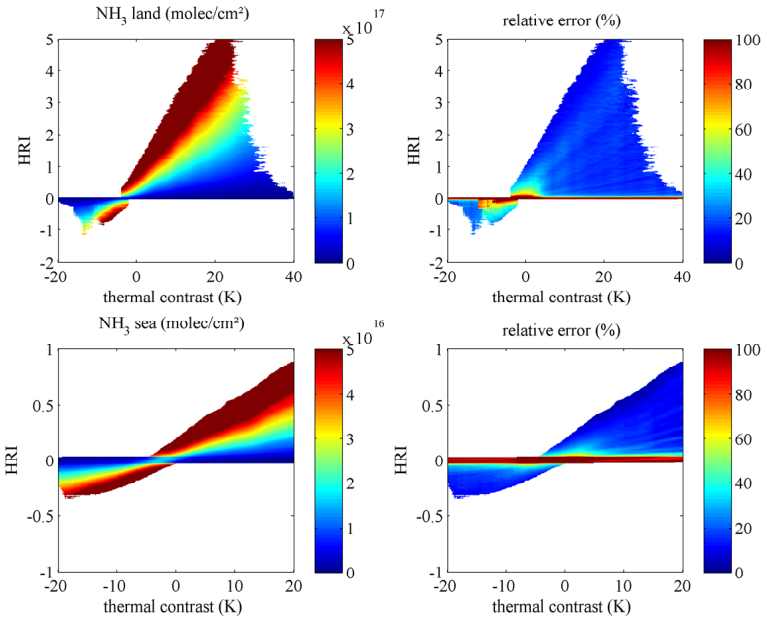

Fig. 4. Look-up tables used to convert *HRI* into NH_3 total columns through the thermal contrast (left) with the associated retrieval error (right), above land (top) and sea (bottom). The tables which are built from about 450 000 simulated IASI spectra above land and 11600 above sea; see text for details.

ACPD
13, 24301–24342, 2013

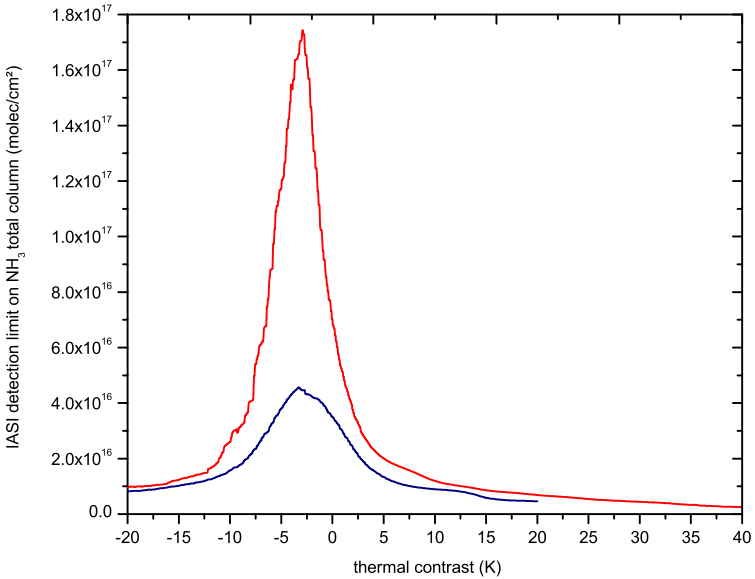

Fig. 5. Lowest possible detectable NH_3 total column, in molec cm^{-2}, above land (red) and sea (blue). The values are those for which the retrieved column would be significant below 2σ in *HRI*.

ACPD
13, 24301–24342, 2013

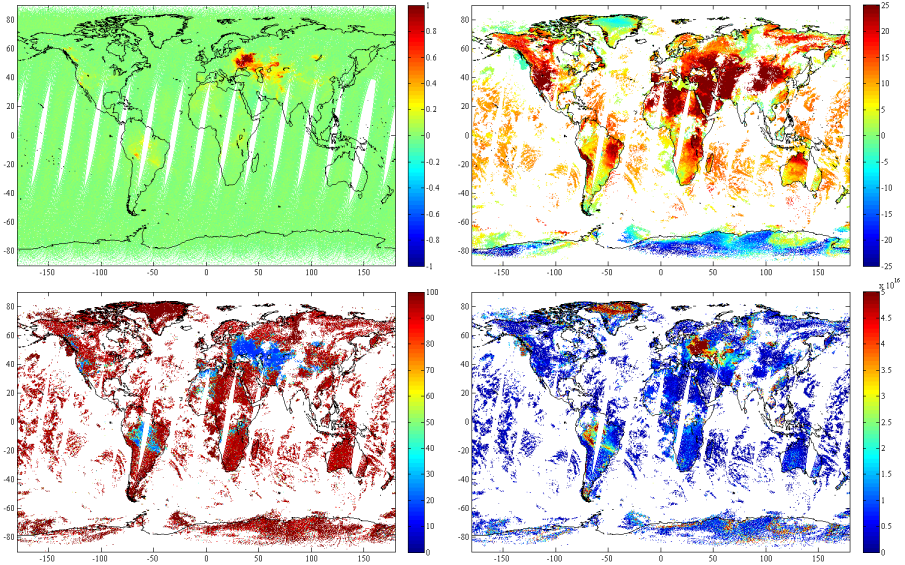

Fig. 6. From top to bottom and from left to right: *HRI* (no unit), thermal contrast (K), relative error (%) and NH_3 total columns (molec cm^{-2}) with posterior filtering, for 15 August 2010 in the morning, as in Fig. 2. The filtering applied here (apart from the *HRI*) removes all points with a cloud fraction above 25 % and a surface temperature below 265.15 K.

ACPD
13, 24301–24342, 2013

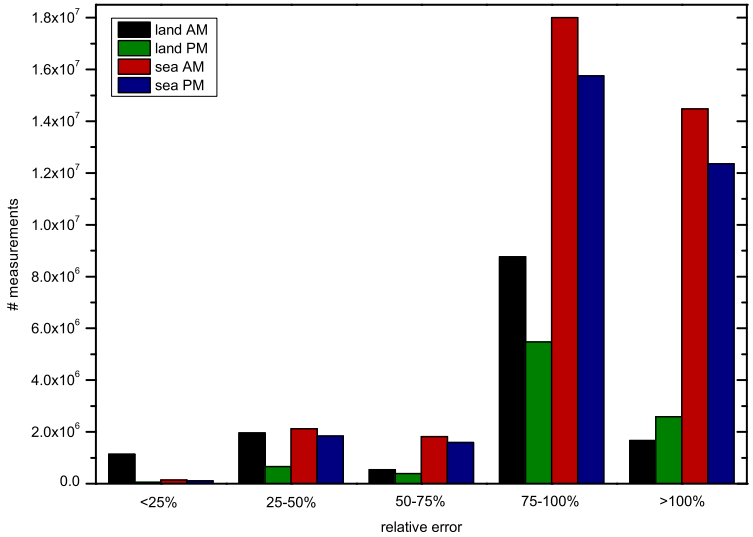

Fig. 7. Number of IASI NH_3 measurements with relative errors on the total column in the range 0–25, 25–50, 50–75, 75–100 and above 100 % over five years (from 1 November 2007 to 31 October 2012).

ACPD
13, 24301–24342, 2013

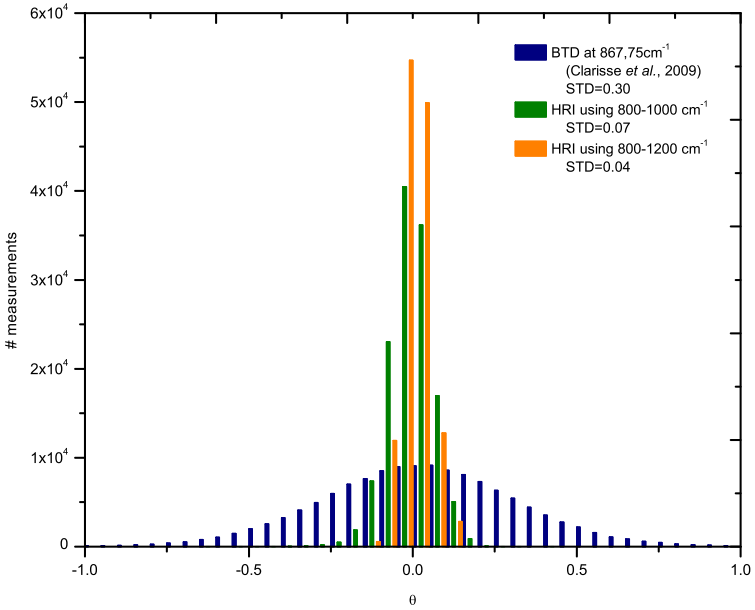

Fig. 8. Histogram of the Θ values of the new retrieval scheme (orange), for a smaller hyperspectral range (green) and for a brightness temperature difference detection method (Clarisse et al., 2009) (blue) for 15 August 2010 (morning overpass). The standard deviation (STD) of Θ values associated with each approach shows the gain of sensitivity of this work using the *HRI* based retrieval scheme.

ACPD
13, 24301–24342, 2013

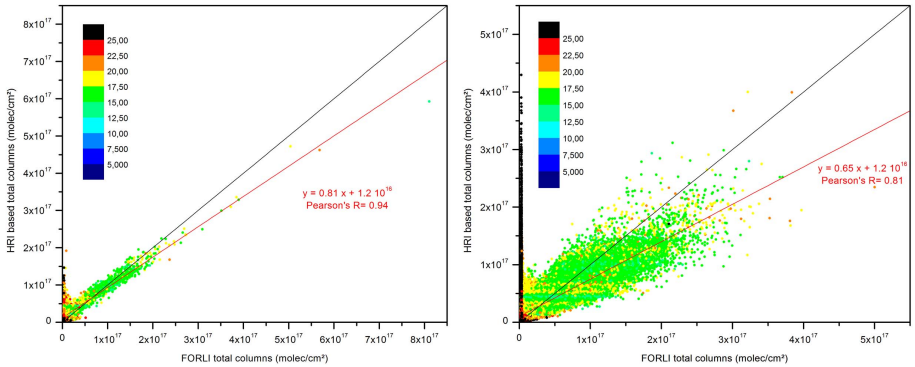

Fig. 9. NH_3 total columns in molec cm^{-2} retrieved in this work from the *HRI* retrieval scheme (y axis) versus those retrieved by FORLI (x axis) for 15 August 2010 (left) and over the entire year 2011 (right). The colors refer to the error calculated with the *HRI* retrieval scheme. The black line represents the 1:1 line and the red line the linear regression weighted by the *HRI* retrievals error. The Pearson's R coefficient, the values of slope and intercept from the linear regression are also given.

ACPD
13, 24301–24342, 2013

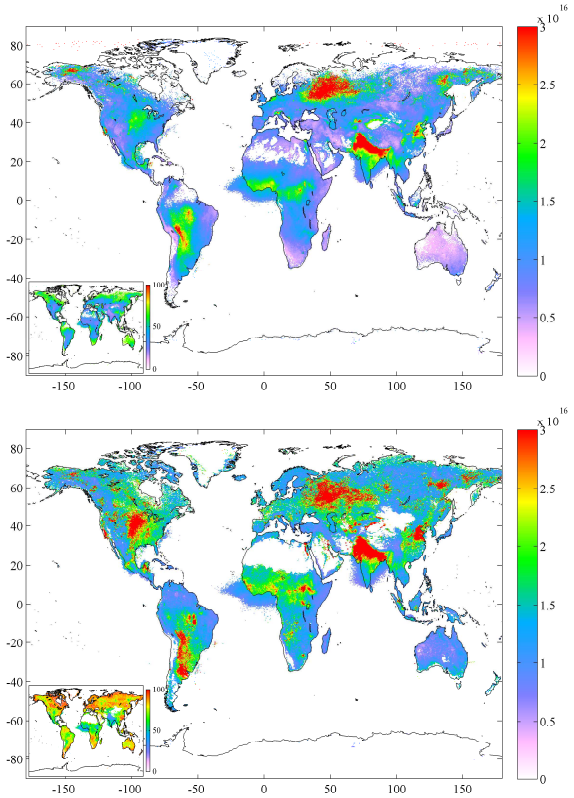

Fig. 10. NH_3 total columns (molec cm^{-2}) and relative error (bottom-left inset, %) distributions for five years of IASI measurements (1 November 2007 to 31 October 2012), in 0.25° × 0.5° cells for the morning (top) and evening (bottom) overpasses. The NH_3 distributions are a mean of all measurements within a cell, weighted by the retrieval error following Eq. (3).The error distributions are a weighted mean of the error of all observations within a cell, following Eq. (4).

ACPD
13, 24301–24342, 2013

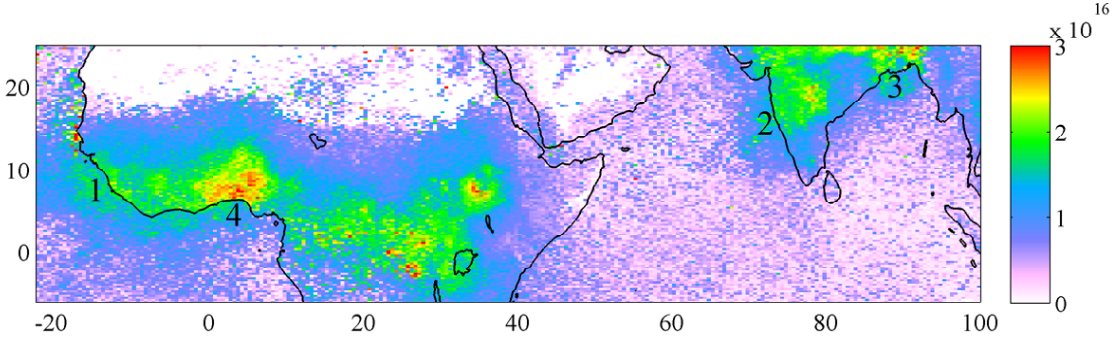

Fig. 11. NH_3 total columns (molec cm^{-2}) distribution averaged for February 2011. A post-filtering has been carried out excluding columns with a mean error above 100 %. Transported NH_3 is observed mainly from fire plumes on the West and South coast of West Africa (1), and mainly from agricultural sources on the West coast of India (2), the Bay of Bengal (3) and the Gulf of Guinea (4).

ACPD
13, 24301–24342, 2013

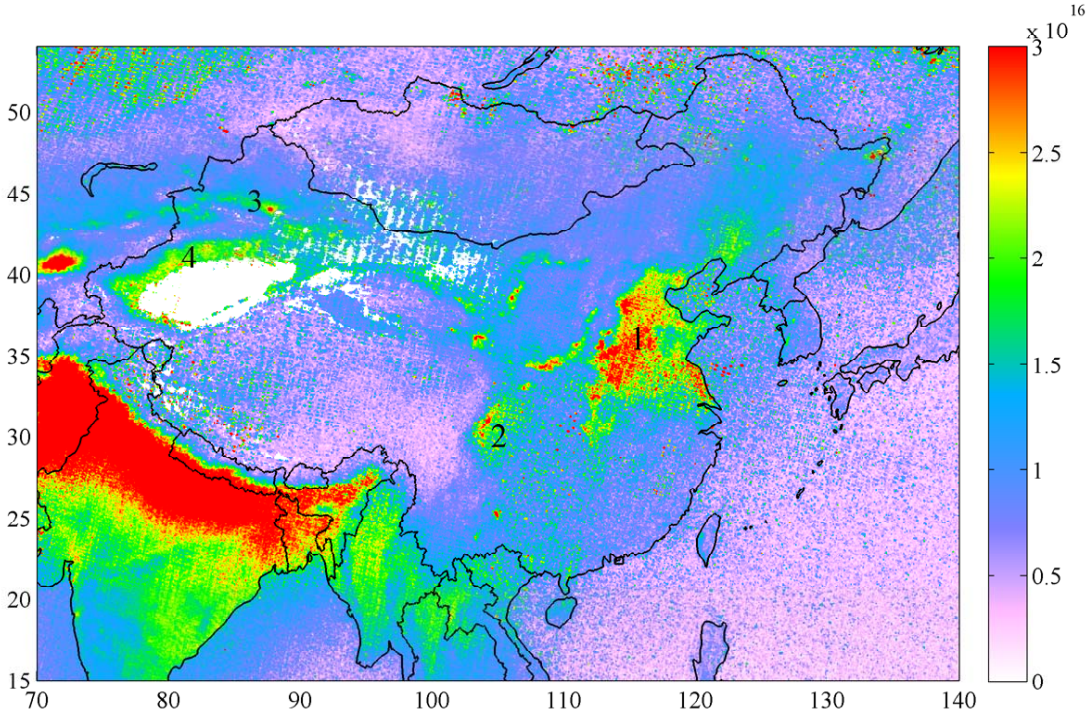

Fig. 12. NH_3 distribution over East Asia (molec cm^{-2}) following a griding method explicitly accounting for the IASI footprint on each individual measurement. The distribution is a five year error-weighted average of the IASI daytime total columns in the region (a post-filtering excluding cells with less than 10 observations has been carried out over land).

ACPD
13, 24301–24342, 2013

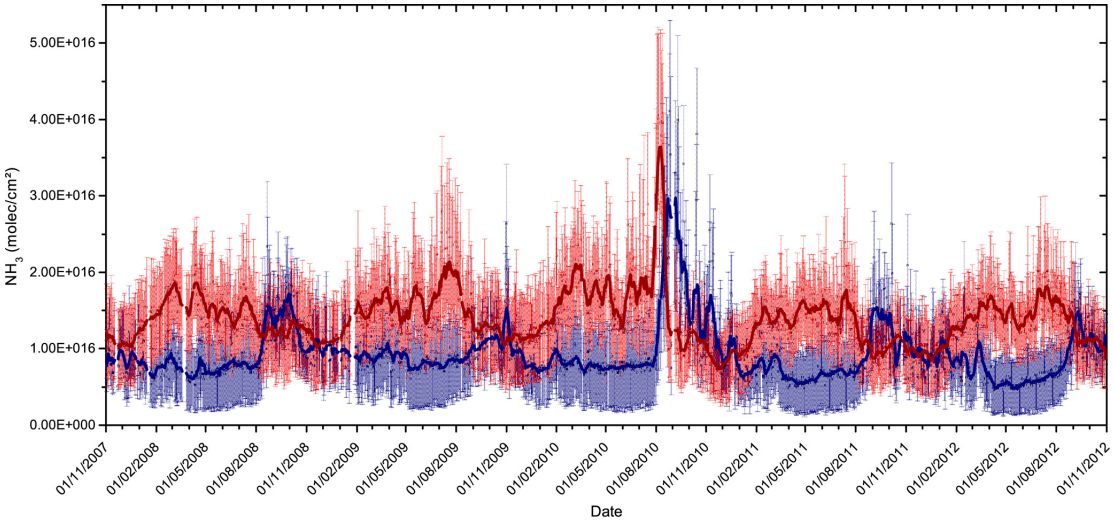

Fig. 13. Time series of day-time NH_3 total columns above land, averaged each day separately over the Northern (NH, red) and the Southern (SH, blue) Hemispheres. The error bars correspond to the error calculated as Eq. (4) around the daily mean value. The red and blue lines are 11-day running means.

ACPD
13, 24301–24342, 2013